AGU PUBLICATIONS

Geophysical Research Letters

RESEARCH LETTER
10.1002/2015GL064281

Key Points:
- A barrier may induce supershear ruptures
- Supershear duration is proportional to the reduction in main rupture speed
- It is critical for a barrier to stop or induce supershear ruptures

Supporting Information:
- Figures S1–S4

Correspondence to:
H. Yang,
hyang@cuhk.edu.hk

Citation:
Weng, H., J. Huang, and H. Yang (2015), Barrier-induced supershear ruptures on a slip-weakening fault, *Geophys. Res. Lett.*, *42*, doi:10.1002/2015GL064281.

Received 18 APR 2015
Accepted 29 MAY 2015
Accepted article online 3 JUN 2015

Barrier-induced supershear ruptures on a slip-weakening fault

Huihui Weng[1,2], Jinshui Huang[1], and Hongfeng Yang[2]

[1]School of Earth and Space Sciences, University of Science and Technology of China, Hefei, China, [2]Earth System Science Programme, Faculty of Science, Chinese University of Hong Kong, Shatin, Hong Kong

Abstract Here we investigate the effects of a patch with elevated effective normal stress (barrier) on two-dimensional in-plane supershear rupture propagation on a planar fault from numerical experiments. Our results confirm that the barrier may slow down or stop coseismic ruptures but may also induce supershear ruptures. We demonstrate that the supershear rupture may emerge in a region that is delineated by two approximate linear boundaries. If the barrier size is below the lower boundary, ruptures can overcome the barrier and propagate at subshear speeds. If the barrier size is larger than the upper boundary, ruptures are always stopped by the barrier. Furthermore, we find that the barrier-induced supershear ruptures may eventually slow down into subshear speed, depending on the size and the location of the barrier. The duration of supershear ruptures increases as the barrier sizes grow from the lower to the upper boundary, which are proportional to the reduction in rupture speeds caused by the barrier. These results indicate that a barrier on the fault may not stop coseismic ruptures. Rather, the barrier may induce ruptures propagating at supershear speeds that play important roles in near-field ground shaking and damage.

1. Introduction

Rupture speeds of earthquakes have significant effects on near-field ground shaking and thus have important implications for assessing seismic risk. Most earthquake ruptures are observed to propagate at speeds lower than the shear wave velocity (V_s), the so-called subshear regime. In contrast, there have been a few reports that the rupture may propagate faster than V_s and thus is called supershear rupture. By far a few earthquakes are named supershear events, such as the 1979 Imperial Valley earthquake [*Archuleta*, 1984], the 1999 Duzce earthquake [*Bouchon et al.*, 2001], the 1999 Kocaeli earthquake [*Bouchon et al.*, 2001], the 2001 Kunlunshan earthquake [*Bouchon and Vallée*, 2003], the 2002 Denali earthquake [*Dunham and Archuleta*, 2004], the 2010 Yushu earthquake [*Wang and Mori*, 2012], and the 2013 Craig earthquake [*Yue et al.*, 2013]. In addition, supershear transition and propagation have also been observed in the laboratory [*Passelègue et al.*, 2013; *Rosakis et al.*, 1999; *Xia et al.*, 2004]. Understanding the mechanism of transitions between subshear and supershear ruptures then becomes a significant problem to better understand earthquake physics.

In general, the supershear transition of mode II crack could be predicted theoretically and numerically under certain conditions. For instance, *Andrews* [1976] has numerically shown that along an unbounded homogeneous fault the supershear transition can occur if a daughter rupture forms ahead of the rupture tip near the peak shear stress that propagates at V_s. In addition, *Dunham* [2007] has suggested that supershear rupture may emerge on homogeneous fault if the value of the nondimensional seismic ratio S is smaller than certain thresholds (1.77 for 2-D bilateral ruptures and 1.42 for unilateral ruptures). Due to effects of free surface, supershear rupture may also emerge at S values higher than the numerical predictions [*Bizzarri*, 2010; *Bizzarri and Das*, 2012; *Kaneko and Lapusta*, 2010; *Zhang and Chen*, 2006]. Furthermore, the presence of favorable heterogeneities, such as a small patch with higher shear stress [*Fukuyama and Olsen*, 2002; *Liu and Lapusta*, 2008], could lead to supershear transition if the heterogeneities are strong enough, similar to asperities that could promote the rupture.

Contrary to the asperities, a patch with elevated effective normal stress on fault could act as a barrier that can slow down or even stop coseismic ruptures [*Duan*, 2012; *Yang et al.*, 2012, 2013]. It has also been suggested that the distance between the barrier and the nucleation zone (NZ) plays a significant role in rupture propagation and termination [*Yang et al.*, 2012, 2013]. However, a barrier may also lead to transient supershear rupture because of high slip velocity pulse emitted from the barrier and/or the split front

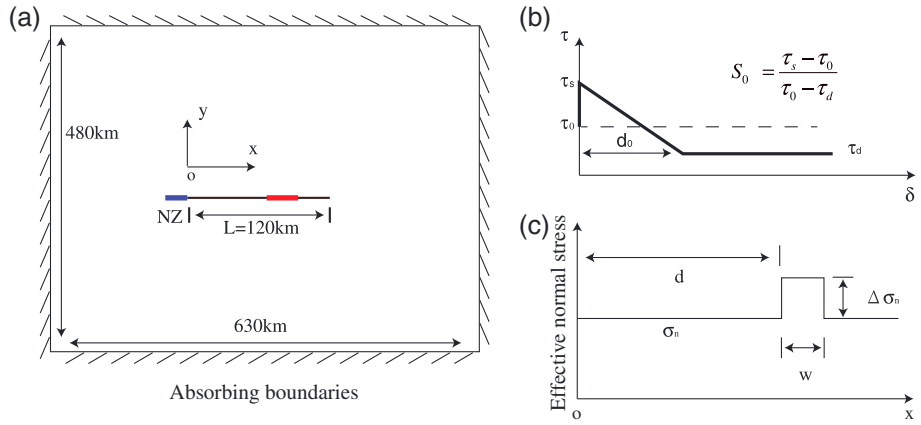

Figure 1. (a) A fault (black line) embedded in an elastic domain with absorbing boundaries. Blue and red lines denote the nucleation zone (NZ) and a barrier. (b) Initial, static, and dynamic stress on the fault. S_0 is the nondimensional seismic ratio. (c) Schematic plot of effective normal stress, σ_n, on the fault. $\Delta\sigma_n$ is the additional effective normal stress. Barrier-NZ distance and the width of the barrier are d and w, respectively.

focusing effect in numerical experiments where the barrier is fixed relative to the NZ [*Dunham et al.*, 2003]. Would the barrier-NZ distance, as well as other factors, affect the supershear transition? Motivated by recent observational and numerical results, we here investigate the effects of a barrier on the supershear transition process.

2. Method

We consider a 2-D in-plane unilateral rupture on a strike-slip fault embedded in a homogeneous elastic space (Figure 1a). To minimize the waves reflected from the boundaries, we set up a sufficiently large domain (480 by 630 km) and apply absorbing boundary conditions by placing dashpots on all boundaries [*Aagaard et al.*, 2012]. The seismogenic fault locates in the center of the domain and extends 120 km along the x axis (Figure 1a). To focus on the effects of frictional heterogeneity on ruptures, the material properties are kept constant for all the simulated models: $V_P = 5.77$ km/s, $V_S = 3.33$ km/s, shear modulus $\mu = 30$ GPa, and Poisson's ratio $v = 0.25$.

The fault is governed by a linear slip-weakening friction law [*Ida*, 1972], one of the most widely used constitutive laws in earthquake source dynamic studies [e.g., *Bizzarri*, 2011]. In the linear slip-weakening law, the shear stress is given by

$$\tau(\delta) = \begin{cases} \sigma_n[f_s - (f_s - f_d)\delta/d_0] & \delta \le d_0 \\ \sigma_n f_d & \delta > d_0 \end{cases} \quad (1)$$

where σ_n is the effective normal stress, f_s is the static friction coefficient, f_d is the dynamic friction coefficient, δ is fault slip, and d_0 is the characteristic slip-weakening distance (Figure 1b). Except for the initial shear stress τ_{nucl} within the NZ that is slightly higher than the static strength (Table 1), f_s, f_d, d_0, and τ_0 are all uniform on the fault. Here we choose a uniform ambient effective normal stress for simplicity (e.g., $\sigma_n = 50$ MPa) and do not incorporate any potential pore pressure changes induced by dilatancy or thermal pressurization during ruptures [*Liu*, 2013; *Segall et al.*, 2010; *Noda and Lapusta*, 2010]. The nucleation zone is set as 3 km in length, whose size is

Table 1. Fault Parameters Used in Simulations

Parameter	Value
Static friction coefficient, f_s	0.630
Dynamic friction coefficient, f_d	0.525
Effective normal stress, σ_n (MPa)	50
Initial shear stress, τ_0 (MPa)	28
Static friction, τ_s (MPa)	31.5
Dynamic friction, τ_d (MPa)	26.25
Initial seismic ratio, S_0	2.0
Shear stress within nucleation zone, τ_{nucl} (MPa)	31.7
Critical slip distance, d_0 (m)	0.40

just over the theoretical estimate of crack length required for instability [*Uenishi and Rice*, 2003]. Numerical simulations of dynamic ruptures are conducted using a finite element code, PyLith [*Aagaard et al*., 2012].

For the linear slip-weakening law in 2-D cases, the rupture cohesive zone must span at least three to five grids to adequately resolve the rupture information [*Day et al*., 2005]. For the parameters given in Table 1, the size of the cohesive zone in this study is ~2.6 km according to the following formula [*Day et al*., 2005]:

$$\Lambda_0 = \frac{9\pi}{32}\frac{\mu}{1-\nu}\frac{d_0}{\tau_s - \tau_d} \tag{2}$$

where τ_s and τ_d are static and dynamic shear stresses, respectively. The grid size Δx is set to be 100 m, and thus, $\Lambda_0/\Delta x = 26$, much larger than the minimum requirement. The time step Δt is 0.005 s, and thus, the Courant-Friedrichs-Lewy ratio, $CFL = V_p \Delta t/\Delta x = 0.29 < 0.71$, satisfies the CFL condition and ensures the stability of the numerical solution [*Mitchell*, 1976]. We define the rupture tip of slip rate exceeding a threshold value, 10^{-4} m/s, and compute the rupture speed using the two-point central difference method by estimating the tip advance over a fixed time interval $\Delta t = 1$ s [e.g., *Liu et al*., 2014].

In this study, a barrier is characterized by three parameters: its distance to the NZ d, its width w, and the additional effective normal stress $\Delta\sigma_n$ (Figure 1c), similar to *Yang et al.* [2013]. To get more insights into the rupture physics, we normalize the distance and the width of the barrier to $d^* = d/\Lambda_0$ and $w^* = w/\Lambda_0$, respectively. In addition, the time t is normalized as $T^* = tV_s/w$, where the time scales are different for barriers with different widths. We change d^* from 19.2 (50 km) to 34.6 (90 km), w^* from 0.38 (1 km) to 5.38 (14 km). In order to better depict the approximate boundaries of supershear transition, we compute more cases near the boundaries. In total, we have computed >700 models, each of whom takes ~1 h on a Linux workstation with 12 cores and 6 Gb memory.

3. Results

We find that the barrier with elevated effective normal stress can induce supershear ruptures. Let us first consider a barrier with a width of $w^* = 1.92$ (i.e., 5 km in our model), a distance of $d^* = 26.9$ (i.e., 70 km), and $\Delta\sigma_n/\sigma_n = 16\%$. As shown in Figure S1 in the supporting information, the rupture starts from the NZ and gradually accelerates into a steady speed ($V_R = 0.92V_s$). When the rupture propagates into the barrier, the rupture slows down but does not completely stop. As the rupture tip gets close to the farside boundary of the barrier, a daughter rupture emerges near the barrier at the farside (Figure 2a). When the barrier is finally broken, the daughter rupture accelerates to a speed higher than V_s, reaching the supershear regime (Figures 2a and S1). After the rupture propagates at supershear speeds for ~6 s, the rupture slows down and then finally propagates at a subshear speed (Figure S1).

To investigate the emergence of the supershear rupture induced by the barrier, we track the history of shear stress on the fault and calculate the dynamic seismic ratio S, which reflects the evolution of shear stress (Figure 2b). As the rupture approaches a point in front of the barrier (e.g., point A), the shear stress slightly decreases and then rapidly increases to the static strength (Figure 2a). Corresponding to the change in shear stress, the dynamic seismic ratio S increases slightly and then quickly drops to zero when this point is ruptured, i.e., $\tau = \tau_s$ (Figure 2b). When the rupture propagates into the barrier, shear stress in the barrier (e.g., point B) first decreases due to the barrier-induced "stopping phase," i.e., a trough in shear stress, propagating at V_s ahead of the rupture tip. Then the shear stress increases after the stopping phase passes by (Figure 2a). Consequently, the S value at the point B is elevated to a large value and then descends to zero when this point slips (Figure 2b). Even though the rupture tip has not propagated out of the barrier, the shear stress at the farside of the barrier is first decreased due to the stopping phase and then increases to the static strength on the fault, initiating a daughter rupture (Figure 2a). The main rupture is halted by the barrier and yet propagates forward. When the barrier is eventually broken, the daughter rupture accelerates into supershear regime (Figure 2a).

By tracking the dynamic seismic ratio S, we find that the S value stays low (e.g., <0.7) for nearly 1 s at the farside before the rupture front arrives (Figure 2b). For instance, shear stress at the point C decreases due to the stopping phase and therefore the dynamic S value at this point is large. Then the S value descends as the shear stress increases after the passage of the stopping phase. Prior to rupture at the point C, the S

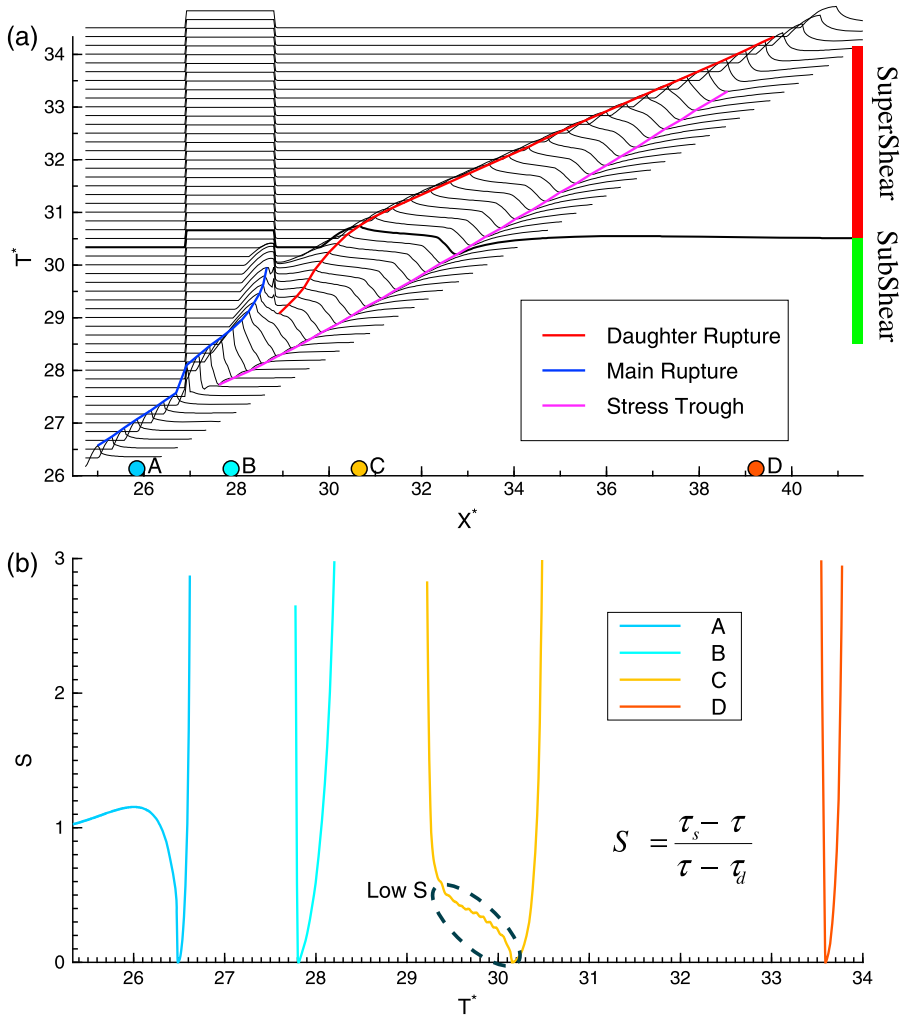

Figure 2. (a) Shear stress history on the fault for a model with $d^* = 26.9$ and $w^* = 1.92$. T^* denotes the normalized time, and x^* represents the nondimensional fault length. Blue and red lines delineate rupture tips of the main and the daughter ruptures. Pink line denotes the stress trough. Red and green bars indicate supershear and subshear propagation regimes. Color dots mark the positions of four points on the fault. (b) The dynamic seismic ratio S versus time at the four positions in Figure 2a. The dashed ellipse indicates the duration of low S value.

value stays low (<0.7) for nearly 1 s due to the gradual ramp of high shear stress behind the stoppingphase (Figure 2), which is favorable for generation of supershear rupture. As a result, the daughter rupture behind the barrier initiates, accelerates, and reaches supershear speed after the point C is ruptured (Figure 2a). Since the supershear rupture propagates faster than the stopping phase (pink line in Figure 2a), the daughter rupture begins to catch up the stopping phase, reducing the length of the gradual ramp in shear stress between them and hence the duration of low S value. After the rupture overtakes the stopping phase (Figure 2a), duration of such low S value reduces, no longer satisfying the propagation of supershear rupture (e.g., point D). Therefore, the rupture slows down and finally propagates at a subshear speed (Figure S1).

In addition to the barrier-induced supershear rupture, we find that the barrier-NZ distance d^* plays a significant role in the supershear transition. If d^* is too small, a rupture cannot overcome the barrier and thus is stopped, e.g., $d^* = 23.1$ (Figures 3a and 3c). In stark contrast, instead of stopping the ruptures at larger d^* values (e.g., $d^* = 26.9$ and 30.8), the rupture propagates at supershear speeds after overcoming the barrier (Figure 3d). In order to investigate the effects of d^* on stopping or inducing supershear ruptures, we track the slip rate on the fault. The maximum slip rate at a point in the barrier becomes larger

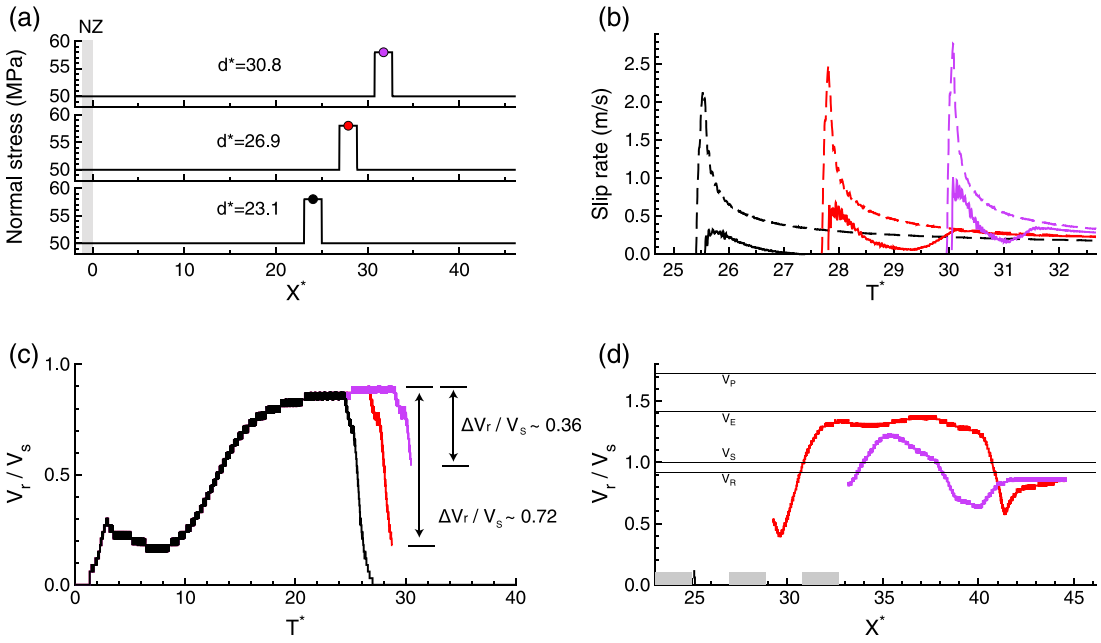

Figure 3. (a) Light bars represent the nucleation zone. The width ($w^* = 1.92$) and the strength ($\Delta\sigma_n/\sigma_n = 16\,\%$) of the barrier are indicated by normal stress (black lines). Color dots mark the midpoint of the barrier. (b) Slip rate history (solid lines) for the three positions shown in Figure 3a, with colors corresponding to the locations ($d^* = 23.1$, 26.9, and 30.8). Dashed color lines show the slip rate history at the same locations without the barrier. (c) Change in the main rupture speed, V_r/V_s with colors corresponding to the different locations of the barrier. (d) Rupture speed history of the daughter ruptures with colors corresponding to the different locations of the barrier. Gray bars indicate location and width of the barrier. Wave velocities of Rayleigh (V_R), shear (V_s), and compressional (V_P) waves are shown. $V_E = \sqrt{2}V_s$.

as the d^* increases (Figure 3b). For instance, the maximum slip rate in the barrier is ~0.3 m/s for $d^* = 23.1$, nearly as half as the one in the case of $d^* = 26.9$ (Figure 3b). Even if we consider the reference case without barrier, the maximum slip rate on the fault increases as d^* becomes larger (Figure 3b). In other words, the rupture tip is more energetic as it propagates further and becomes more difficult to stop.

We then investigate all our simulation cases and find that if the distance d^* is too small, e.g., <20.8 (i.e., 54 km in our model), supershear transition does not occur (Figure 4). Ruptures either overcome the barrier or are stopped, depending on the size and the strength of the barrier. However, supershear transition always emerges if d^* is larger than ~21.2 (i.e., 55 km in our model). Furthermore, as d^* increases, the propagation distance of the supershear rupture decreases (Figure 3d). For instance, the distance of supershear propagation is ~9.23 (i.e., 24 km) for $d^* = 26.9$, larger than the supershear distance (~7 km) for $d^* = 30.8$. In addition, we find that the reduction in rupture speeds ΔV_r caused by the barrier is also relevant to d^*. For a barrier with identical width and strength, the larger the d^* is, the smaller the ΔV_r is. For instance, ΔV_r is 0.72 for $d^* = 26.9$ and is 0.36 for $d^* = 30.8$.

In addition to the d^*, the size of the barrier, w^*, also plays a critical role in the supershear transition as well as the propagation distance of the supershear rupture (Figure 4a). If the barrier is too large, it will always stop ruptures. If the barrier is very small, ruptures can always overcome the barrier but cannot accelerate into supershear speed (Figure 4a). The supershear transition only occurs for certain ranges of d^* and w^*, forming a region with two approximately linear boundaries (Figure 4a). The upper boundary separates the cases of all stopped ruptures and the supershear transition. The lower boundary divides the subshear and supershear rupture speeds.

The propagation distance of the supershear rupture increases from the lower boundary to the upper boundary; i.e., for a fixed d^*, the duration of the supershear rupture increases as the w^* becomes larger (Figure 4a). All the largest propagation distances of supershear ruptures occur near the upper boundary, which delineates a critical condition for the barrier to stop or to induce strong supershear ruptures. For an extreme case of $d^* = 34.6$ and $w^* = 2.92$, the rupture quickly accelerates into supershear and then

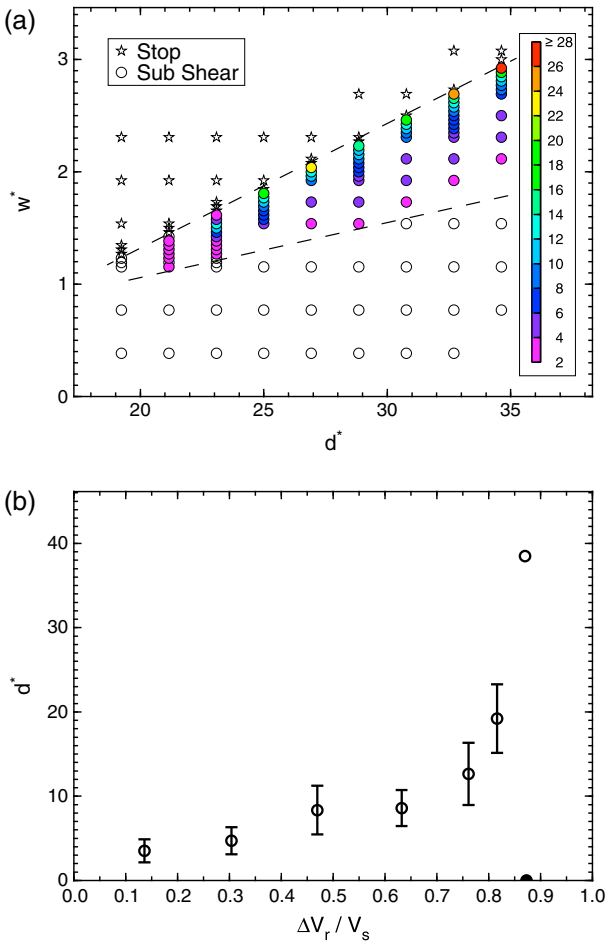

Figure 4. (a) Effect of barriers on rupture propagation ($\Delta\sigma_n/\sigma_n$) = 16 %. Rupture stopped by the barrier (star) or overcome the barrier (circle). Colors indicate the nondimensionalized propagation distance of the supershear rupture. Two dashed lines denote approximate boundaries of the supershear regime with supershear propagation distance larger than 5 km. (b) The normalized propagation distance of supershear rupture as a function of the reduction in the main rupture speed. Error bars show 95% confidence interval calculated for all simulated cases at the same ΔV_r.

propagates on the entire fault at a speed between V_E (i.e., $\sqrt{2}V_s$) and V_P, producing the largest propagation distance of supershear ruptures in our experiment. To verify that this long-lasting supershear rupture is not limited by our domain size, we increase fault length from 120 km to 200 km and the corresponding domain. We find that the rupture continues to propagate on the fault at supershear speed, even after it overtakes the stopping phase (Figures S2 and S3).

4. Discussion

It has been shown that a barrier with additional strength could cause supershear ruptures in the previous 3-D numerical studies [*Dunham et al.*, 2003; *Bizzarri et al.*, 2010]. For instance, *Dunham et al.* [2003] characterize the barrier as a circle patch with higher static friction. The dynamic friction and the initial shear stress in the barrier are identical to the ambient fault. Supershear rupture is generated when the barrier is broken, emitting a high slip pulse that scales linearly with dynamic stress drop. If the barrier strength is extremely high, e.g., 600% higher than the ambient fault, the barrier is unbroken. But supershear rupture may still emerge by the focusing effect of concave rupture front. Although we have observed the similar supershear transition induced by a barrier, the mechanism of supershear transition in our study seems different than what was reported in *Dunham et al.* [2003]. First, there is no rupture front focusing effect in our 2-D model as the rupture front cannot bypass the barrier. Second, we do not observe high slip pulse emitted from the broken barrier because we did not introduce additional dynamic stress drop in the barrier. The barrier-induced supershear transitions in our simulated cases are attributed to the low dynamic seismic ratio S, which are generated by the barrier-induced stopping phases that propagate at V_s (Figure 2). Since the rupture is slowed down by the barrier, the distance between the stopping phase and the rupture front is elongated, making a long ramp for shear stress to grow (Figure 2a). Therefore, the S value stays low and creates a favorable condition for supershear ruptures. Furthermore, we observe the smooth transition of rupture speed across the forbidden zone, i.e., speed between Rayleigh and shear wave velocities (Figure 3d). This is also attributed to the low S value ($<$0.7), as it has been pointed out that the weaker fault with low S value less than 0.72 would produce smooth rupture acceleration across the forbidden zone [*Liu et al.*, 2014].

Our results indicate that although the supershear transition may occur, the rupture speed may drop back to subshear regime, depending on the size and the location of the barrier. In other words, the supershear transition may be transient and the duration of supershear propagation is proportional to the reduction in rupture speed ΔV_r induced by the barrier (Figure 4b). Since the stopping phase propagates at V_s, the

distance between the stopping phase and the rupture front increases if ΔV_r is larger. It requires more time (i.e., longer distance) for the rupture front to catch up the stopping phase, making duration of the supershear longer. *Madariaga* [1983] has proved that the dynamic stress concentration ahead of the rupture tip increases as ΔV_r increases. Thus, the larger the ΔV_r is, more energy is transmitted forward to produce a stronger supershear rupture. Such transient supershear rupture has been reported in field observations, e.g., the 1979 Imperial Valley earthquake [*Archuleta*, 1984]. The kinematic source model of this earthquake suggests that the rupture initially accelerated to a nearly constant subshear speed, slowed down slightly, followed by an abrupt acceleration into supershear regime, and then rapidly decelerated to subshear speed after a short distance [*Archuleta*, 1984]. Despite the uncertainties in the rupture process inferred from seismic observations, our numerical results are qualitatively consistent with the variation of rupture speed of the 1979 Imperial Valley earthquake, providing a plausible mechanism for transient supershear rupture.

Furthermore, we find that the supershear rupture speeds are also dependent on ΔV_r (Figure S2). For most cases, the speeds of supershear ruptures are less than ~1.5 V_s, and the ruptures decelerate into subshear speeds when they overtake the stopping phase. If ΔV_r is sufficiently large, the speed of the supershear rupture is also high (e.g., larger than ~1.5 V_s). Then the rupture is not slowed down to subshear speed but propagates at supershear speed on the entire fault (Figures S2 and S3). For example, we observe such a case for $d^* = 34.6$ and $w^* = 2.92$, in which the rupture propagates at a speed of ~5 km/s for more than 120 km (Figures S2 and S3). Our numerical results are similar to seismic observation of the rupture process of the 2001 Kunlunshan earthquake, whose rupture propagated at sub-Rayleigh speeds for the first 100 km and then became supershear with an approximate speed of 5 km/s [*Bouchon and Vallée*, 2003].

If ΔV_r is even larger, the ruptures will be stopped by the barrier (Figure 4). Because the slip rates inside the barrier are already critically low for these strongest supershear cases, any additional resistance of the barrier (either strength or width) will stop the ruptures. Consequently, there is a sharp boundary for the barrier to stop or to induce strongest supershear ruptures (Figure 4). For the same distance, there is a trade-off between the width w^* and the relative strength $\Delta\sigma_n/\sigma_n$ for stopping ruptures [*Yang et al*., 2013]. Tests show there is also a trade-off between w^* and $\Delta\sigma_n/\sigma_n$ for inducing supershear transition (Figure S4). However, the main conclusions of this study still holds for different $\Delta\sigma_n/\sigma_n$ except that the critical width w^* for supershear transition decreases as $\Delta\sigma_n/\sigma_n$ increases.

In our numerical experiments, we have ignored a few factors that play important roles in rupture propagation and termination, such as geometry [e.g., *Yang et al*., 2013], fluid effects [e.g., *Liu*, 2013; *Segall et al*., 2010; *Noda and Lapusta*, 2010], and material contrast across the fault interface [e.g., *Harris and Day*, 2005; *Yang and Zhu*, 2010; *Yang et al*., 2014; *Yang*, 2015]. For instance, *Yang et al.* [2013] have shown that a geometrical patch may stop ruptures even with reductions in effective normal stress. In addition, the material contrast across the fault interface may have important effects on the rupture speed and preferred rupture direction [e.g., *Harris and Day*, 2005; *Shi and Ben-Zion*, 2006]. Furthermore, we did not consider different nucleation procedures that may affect the rupture speed [e.g., *Bizzarri*, 2010; *Liu and Lapusta*, 2008; *Lu et al*., 2009]. In particular, it has been noted that improper nucleation procedure may induce improper supershear rupture propagation in the conditions where the subshear regime is allowed [*Bizzarri*, 2010]. In our numerical experiments, we have carefully set up the initial conditions to ensure that the rupture propagation is adequately resolved. Although these ignored factors may probably change the values of the propagation distance of the supershear rupture and the rupture speed that are reported in this study, our main conclusions of effects on supershear transition of barrier size and barrier-NZ distance will still hold.

5. Conclusions

Our numerical results show that a barrier on the fault may not always stop coseismic ruptures but may rather induce supershear ruptures. The supershear ruptures are promoted by a long duration of low dynamic seismic ratio S that is caused by the stopping phase generated by the barrier. The barrier will also cause a reduction in rupture speed, ΔV_r, which appears to control the propagation distance of the supershear rupture. In addition, we find that the condition for the barrier to stop ruptures or induce supershear ruptures is rather critical, as indicated by the sharp upper boundary (Figure 4). Variation of rupture speeds in our findings is qualitatively consistent with seismic observations, providing a plausible mechanism of

occurrence of supershear earthquakes. If this is the case in the field, we should expect to observe fault heterogeneities around where the rupture speeds accelerate to supershear. Deriving high-resolution structure of fault zones using dense across-fault arrays is desired to investigate such heterogeneities [e.g., *Yang et al*., 2011, 2014] and then to advance our understanding of fault zone evolution and earthquake generation.

Acknowledgments

H. Weng and H. Yang are supported by Yang's startup fund (grant 4930072) and Direct Grant for Research (grant 4053114) from the Chinese University of Hong Kong. This work is also supported by National Science Foundation of China (grants 41474082 and 91014005). All data used in this study are generated from numerical simulations. All figures are produced using Generic Mapping Tools (GMT). We are grateful to Brad Aagaard for his help on using the finite element code, PyLith. We thank Associate Editor Michael Wysession and two anonymous reviewers for their constructive comments that help improve the paper.

The Editor thanks two anonymous reviewers for their assistance in evaluating this paper.

References

Aagaard, B., S. Kientz, M. G. Knepley, S. Somala, L. Strand, and C. Williams (2012), PyLith user manual, version 1.7.1, Computational Infrastructure for Geodynamics (CIG), Univ. of California, Davis, Calif. [Available at http://www.geodynamics.org/cig/software/pylith/pylith_manual-1.7.1.pdf, Last accessed 6 May 2013.]

Andrews, D. J. (1976), Rupture velocity of plane strain shear cracks, *J. Geophys. Res.*, *81*(32), 5679–5687, doi:10.1029/JB081i032p05679.

Archuleta, R. J. (1984), A faulting model for the 1979 Imperial Valley earthquake, *J. Geophys. Res.*, *89*(B6), 4559–4585, doi:10.1029/JB089iB06p04559.

Bizzarri, A. (2010), How to promote earthquake ruptures: Different nucleation strategies in a dynamic model with slip-weakening friction, *Bull. Seismol. Soc. Am.*, *100*, 923–940, doi:10.1785/0120090179.

Bizzarri, A. (2011), On the deterministic description of earthquakes, *Rev. Geophys.*, *49*, RG3002, doi:10.1029/2011RG000356.

Bizzarri, A., and S. Das (2012), Mechanics of 3-D shear cracks between Rayleigh and shear wave rupture speeds, *Earth Planet. Sci. Lett.*, *357–358*, 397–404, doi:10.1016/j.epsl.2012.09.053.

Bizzarri, A., E. M. Dunham, and P. Spudich (2010), Coherence of Mach fronts during heterogeneous supershear earthquake rupture propagation: Simulations and comparison with observations, *J. Geophys. Res.*, *115*, B08301, doi:10.1029/2009JB006819.

Bouchon, M., and M. Vallée (2003), Observation of long supershear rupture during the magnitude 8.1 Kunlunshan earthquake, *Science*, *301*(5634), 824–826.

Bouchon, M., M. P. Bouin, H. Karabulut, M. N. Toksöz, M. Dietrich, and A. J. Rosakis (2001), How fast is rupture during an earthquake? New insights from the 1999 Turkey earthquakes, *Geophys. Res. Lett.*, *28*(14), 2723–2726, doi:10.1029/2001GL013112.

Day, S. M., L. A. Dalguer, N. Lapusta, and Y. Liu (2005), Comparison of finite difference and boundary integral solutions to three-dimensional spontaneous rupture, *J. Geophys. Res.*, *110*, B12307, doi:10.1029/2005JB003813.

Duan, B. (2012), Dynamic rupture of the 2011 M_w 9.0 Tohoku-Oki earthquake: Roles of a possible subducting seamount, *J. Geophys. Res.*, *117*, B05311, doi:10.1029/2011JB009124.

Dunham, E. M. (2007), Conditions governing the occurrence of supershear ruptures under slip-weakening friction, *J. Geophys. Res.*, *112*, B07302, doi:10.1029/2006JB004717.

Dunham, E. M., and R. J. Archuleta (2004), Evidence for a supershear transient during the 2002 Denali fault earthquake, *Bull. Seismol. Soc. Am.*, *94*(6B), S256–S268.

Dunham, E. M., P. Favreau, and J. Carlson (2003), A supershear transition mechanism for cracks, *Science*, *299*(5612), 1557–1559.

Fukuyama, E., and K. Olsen (2002), A condition for super-shear rupture propagation in a heterogeneous stress field, *Pure Appl. Geophys.*, *159*, 2047–2056.

Harris, R. A., and S. M. Day (2005), Material contrast does not predict earthquake rupture propagation direction, *Geophys. Res. Lett.*, *32*, L23301, doi:10.1029/2005GL023941.

Ida, Y. (1972), Cohesive force across the tip of a longtitudinal-shear crack and Griffith's specific surface energy, *J. Geophys. Res.*, *77*, 3796–3805, doi:10.1029/JB077i020p03796.

Kaneko, Y., and N. Lapusta (2010), Supershear transition due to a free surface in 3-D simulations of spontaneous dynamic rupture on vertical strike-slip faults, *Tectonophysics*, *493*(3), 272–284.

Liu, C., A. Bizzarri, and S. Das (2014), Progression of spontaneous in-plane shear faults from sub-Rayleigh to compressional wave rupture speeds, *J. Geophys. Res. Solid Earth*, *119*, 2047–2056, doi:10.1002/2014JB011187.

Liu, Y. (2013), Numerical simulations on megathrust rupture stabilized under strong dilatancy strengthening in slow slip region, *Geophys. Res. Lett.*, *40*, 1311–1316, doi:10.1002/grl.50298.

Liu, Y., and N. Lapusta (2008), Transition of mode II cracks from sub-Rayleigh to intersonic speeds in the presence of favorable heterogeneity, *J. Mech. Phys. Solid.*, *56*(1), 25–50.

Lu, X., N. Lapusta, and A. J. Rosakis (2009), Analysis of supershear transition regimes in rupture experiments: The effect of nucleation conditions and friction parameters, *Geophys. J. Int.*, *177*(2), 717–732.

Madariaga, R. (1983), High frequency radiation from dynamic earthquake fault models, *Ann. Geophys.*, *1*(1), 17–23.

Mitchell, A. R. (1976), *Computational Methods in Partial Differential Equations*, Wiley, New York.

Noda, H., and N. Lapusta (2010), Three-dimensional earthquake sequence simulations with evolving temperature and pore pressure due to shear heating: Effect of heterogeneous hydraulic diffusivity, *J. Geophys. Res.*, *115*, B12314, doi:10.1029/2010JB007780.

Passelègue, F. X., A. Schubnel, S. Nielsen, H. S. Bhat, and R. Madariaga (2013), From sub-Rayleigh to supershear ruptures during stick-slip experiments on crustal rocks, *Science*, *340*(6137), 1208–1211.

Rosakis, A., O. Samudrala, and D. Coker (1999), Cracks faster than the shear wave speed, *Science*, *284*(5418), 1337–1340.

Segall, P., A. M. Rubin, M. Bradley, and J. R. Rice (2010), Dilatant strengthening as a mechanism for slow slip events, *J. Geophys. Res.*, *115*, B12305, doi:10.1029/2010JB007449.

Shi, Z., and Y. Ben-Zion (2006), Dynamic rupture on a bimaterial interface governed by slip-weakening friction, *Geophys. J. Int.*, *165*, 469–484, doi:10.1111/j.1365-246X.2006.02853.x.

Uenishi, K., and J. R. Rice (2003), Universal nucleation length for slip-weakening rupture instability under nonuniform fault loading, *J. Geophys. Res.*, *108*(B1), 2042, doi:10.1029/2001JB001681.

Wang, D., and J. Mori (2012), The 2010 Qinghai, China, earthquake: A moderate earthquake with supershear rupture, *Bull. Seismol. Soc. Am.*, *102*(1), 301–308.

Xia, K., A. J. Rosakis, and H. Kanamori (2004), Laboratory earthquakes: The sub-Rayleigh-to-supershear rupture transition, *Science*, *303*(5665), 1859–1861.

Yang, H. (2015), Recent advances in imaging crustal fault zones: A review, *Earthquake Sci.*, doi:10.1007/s11589-015-0114-3.

Yang, H., and L. Zhu (2010), Shallow low-velocity zone of the San Jacinto Fault from local earthquake waveform modelling, *Geophys. J. Int.*, *183*(1), 421–432.

Yang, H., L. Zhu, and E. S. Cochran (2011), Seismic structures of the Calico fault zone inferred from local earthquake travel time modelling, *Geophys. J. Int.*, *186*(2), 760–770.

Yang, H., Y. Liu, and J. Lin (2012), Effects of subducted seamounts on megathrust earthquake nucleation and rupture propagation, *Geophys. Res. Lett.*, *39*, L24302, doi:10.1029/2012GL053892.

Yang, H., Y. Liu, and J. Lin (2013), Geometrical effects of a subducted seamount on stopping megathrust ruptures, *Geophys. Res. Lett.*, *40*, 2011–2016, doi:10.1002/grl.50509.

Yang, H., Z. Li, Z. Peng, Y. Ben-Zion, and F. Vernon (2014), Low-velocity zones along the San Jacinto Fault, Southern California, from body waves recorded in dense linear arrays, *J. Geophys. Res. Solid Earth*, *119*, 8976–8990, doi:10.1002/2014JB011548.

Yue, H., T. Lay, J. T. Freymueller, K. Ding, L. Rivera, N. A. Ruppert, and K. D. Koper (2013), Supershear rupture of the 5 January 2013 Craig, Alaska (M_w 7.5) earthquake, *J. Geophys. Res. Solid Earth*, *118*, 5903–5919, doi:10.1002/2013JB010594.

Zhang, H., and X. Chen (2006), Dynamic rupture on a planar fault in three-dimensional half-space—II. Validations and numerical experiments, *Geophys. J. Int.*, *167*(2), 917–932.